Excitation-assisted nonadiabatic charge-transfer reaction in a mixed atom-ion system

Ming Li,[1,*] Michael Mills,[2] Prateek Puri,[2] Alexander Petrov,[1,3] Eric R. Hudson,[2,4] and Svetlana Kotochigova[1]

[1]*Department of Physics, Temple University, Philadelphia, Pennsylvania 19122, USA*

[2]*Department of Physics and Astronomy, University of California, Los Angeles, California 90095, USA*

[3]*NRC Kurchatov Institute PNPI, Gatchina, Leningrad District 188300, and Division of Quantum Mechanics, St. Petersburg State University, St. Petersburg 199034, Russia*

[4]*Center for Quantum Science and Engineering, University of California, Los Angeles, California 90095, USA*

(Received 8 January 2019; published 14 June 2019)

An important physical process unique to neutral-ion systems is the charge-transfer reaction. Here, we present measurements of and models for charge-transfer processes between cotrapped ultracold Ca atoms and Yb ions under well-controlled conditions. The theoretical analysis suggests the existence of three reaction mechanisms when lasers from a magneto-optical trap and an additional catalyst laser are present. We show that the near-degeneracy of the excited $\mathrm{Ca}(^1P_1) + \mathrm{Yb}^+(^2S)$ and $\mathrm{Ca}^+(^2S) + \mathrm{Yb}(^3D_2)$ asymptotic limits leads to large charge-transfer rate coefficients that can be controlled by changing the frequency of the catalyst laser and the ion temperature. Our model agrees with experimental rate-coefficient measurements between 50 mK and 1 K, with and without the catalyst laser, using just a single free parameter.

DOI: 10.1103/PhysRevA.99.062706

I. INTRODUCTION

Over the last few decades the study of individual quantum systems decoupled from external perturbations has become a reality. Combining quantum-degenerate gases of fermionic or bosonic atoms, held in electromagnetic traps with a wide range of geometries, with cooled and trapped ions is an exciting and dynamic area in physics. Cold and trapped atom-ion mixtures can be engineered with a high level of control, detected state selectively, and even constructed at the single-ion level. The majority of experimental and theoretical research on charge transfer (CT) with ultracold atoms and ions has focused on their collisions when prepared in their electronic ground state [1–18]. Often, however, cold atom-ion experiments involve holding the neutral atoms in a magneto-optical trap (MOT), providing opportunities for scattering of electronically excited atoms with the cotrapped ions. Although the first steps towards understanding these collisions have been reported [9,19,20], theoretical details are still poorly understood.

Charge transfer can only be realized through transitions between two or more potential energy surfaces that are characterized by electron transfer from the neutral atom to the ion, i.e., $\mathrm{A}^+ + \mathrm{B} \rightarrow \mathrm{A} + \mathrm{B}^+$. In the conventional Born-Oppenheimer (BO) adiabatic picture, such transitions occur due to nonadiabatic coupling induced by the nuclear motion in the initial and final electronic states [21]. Usually, this coupling occurs in a small localized range of interparticle separations R, when electronic BO potentials of the same symmetry have a so-called avoided crossing following the Wigner-Witmer noncrossing rule.

When an avoided crossing between entrance and exit BO potentials is broad as is the case for many heteronuclear atom-ion pairs in their electronic ground states, the CT rate coefficients are very small, in most cases of the order of 10^{-14} cm^3/s or below [7,18,22,23]. On the other hand, in a region where the molecular structure is complex and potential curves are dense, there is a high probability of having narrower avoided crossings that will lead to much higher CT rate coefficients, sometimes approaching values of universal models [20,24]. Our study provides clear evidence of such a situation when a number of excited states with closely lying potentials, populated through an excitation laser, couple strongly via nonadiabatic couplings leading to significant CT reactions. Even though the atoms in the MOT spend most of their time in the ground electronic state, the rate coefficients can still reach four orders of magnitude higher than that of pure ground-state CT reactions.

Here, we study collisions between Ca atoms in a MOT and Yb^+ ions in a colocated linear-quadrupole ion trap. In this system, CT reactions involve excited $4s4p\,^1P$ Ca atoms and ground-state Yb^+ ions. Experimental and theoretical CT rate coefficients are obtained and compared for temperatures $0.01\ \mathrm{K} < T < 1\ \mathrm{K}$.

We use a coupled-channels (CC) model of atom-ion scattering based on ground- and excited-state diabatic potentials, their couplings, and the infinite-order sudden approximation. The Hamiltonian is the sum of a kinetic and a potential energy operator. The relative kinetic energy operator is inversely proportional to the reduced mass of the dimer based on the masses of the atom and ion (rather than the masses of the nuclei) and captures the dominant nonadiabatic corrections. In principle, the coordinate depends on which of the two atoms is ionized, either $\mathrm{Ca} + \mathrm{Yb}^+$ or $\mathrm{Ca}^+ + \mathrm{Yb}$. These correspond to the separations R_1 and R_2 between the centers of mass of the neutral atom and the ion, respectively. Similarly, the reduced masses of the two collisional complexes, μ_1 and μ_2, are different. However, the differences in R_1 and R_2 and μ_1 and μ_2 are small, of the order of the

*ming.li@temple.edu

electron-to-reduced-dimer mass ratio ($\sim 1/2000$). Therefore, given other approximations within our CC calculations, we chose R and μ as those of the entrance channel $Ca + Yb^+$ throughout the paper.

At each R, the separation between the center of mass of Ca and Yb^+, the potential energy operator can be written in a matrix representation with dimensions given by the number of channels or states (defined in detail in the next two sections). The diabatic potentials correspond to the diagonal matrix elements and couplings are off diagonal matrix elements. Special attention has been given to the long-range induction and dispersion interactions, as the dissociation limits of excited-state potentials are in close proximity and nonnegligible couplings between the potentials are present at relatively large separations.

We incorporate spontaneous emission from excited-state potentials and include survival probabilities as an important element in our model. To further elucidate the role of excited states in CT an additional catalyst laser with a frequency that is red detuned from that of the MOT laser is applied. As we show, the effect of spontaneous emission on the reaction path is then suppressed.

We show that up to three mechanisms or pathways contribute to the reaction outcome. Only the third pathway involves the additional catalyst laser. In the first, an atom in the excited state collides and reacts with the ion. In the second, a ground-state atom in the presence of the long-range interaction from a ground-state ion is resonantly excited by absorption of a photon from the MOT lasers and then reacts with the ion. Finally, for the third pathway a colliding ground-state atom-ion pair absorbs a photon from the tunable catalyst laser and then reacts. In all pathways the long-range interaction potentials between the cold atom and ion together with spontaneous emission from the electronically excited atom-ion complex determine the rate coefficients.

II. MODELING CHARGE-TRANSFER PATHWAYS

A. Molecular complex and pathways

We start our analysis with the potential energy landscape for the excited-state CT reaction. Figure 1(a) shows the relevant long-range diabatic $|\Omega| = 1/2$, $3/2$, and $5/2$ potentials, derived from the multipole expansion of the molecular forces, dissociating to the $Ca(4s4p\,^1P_1) + Yb^+(6s\,^2S)$ limit as well as to the nearly degenerate $Ca^+(4s\,^2S) + Yb(5d6s\,^3D_2)$ limit. Their asymptotic splitting is only $\Delta = hc \times 37.7\ \mathrm{cm}^{-1}$, where h is the Planck constant and c is the speed of light in vacuum. Moreover, the molecular electronic state of each diabatic potential is a unique element of the separation-independent "atomic basis" of products of the relevant atomic or ionic Ca and Yb states. The projection of the total electron angular momentum on the internuclear axis, Ω, is a good quantum number. Charge transfer only occurs between states with the same Ω, which for our system occurs for $|\Omega| = 1/2$ potentials near the two crossings at $R \approx 40a_0$, where a_0 is the Bohr radius. Spin-orbit couplings are included which are essential for the exit channels dissociating to the $Ca^+(4s\,^2S) + Yb(5d6s\,^3D_2)$ limit. Details of our calculation of the potentials and, in particular, the evaluation of the strength of the coupling near the crossing points can be found below as well as in Appendix A.

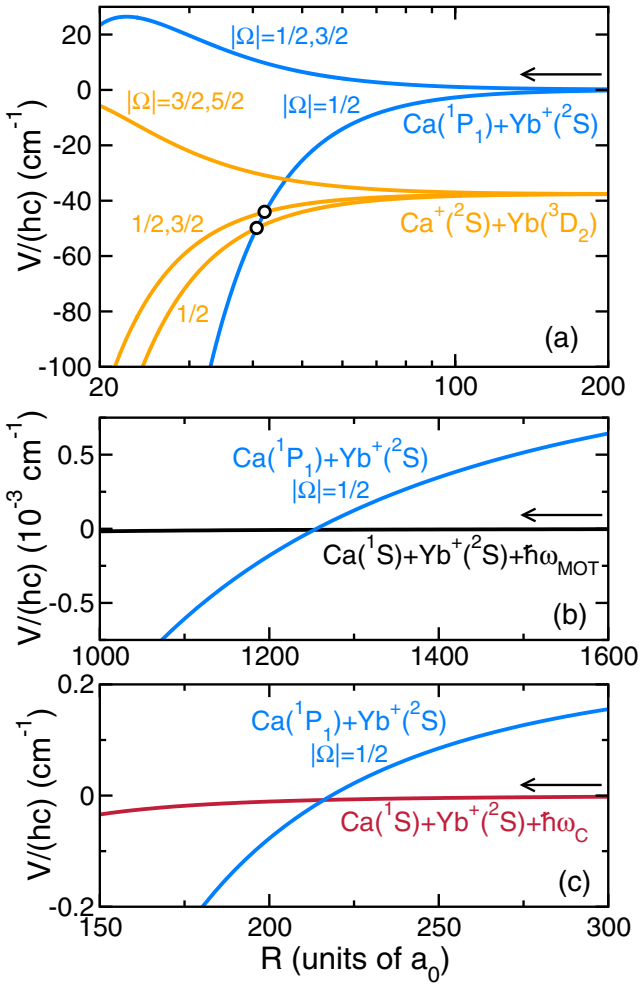

FIG. 1. (a) Long-range diabatic potential energy curves in the atomic basis as functions of the atom-ion separation R on a logarithmic scale. Blue and orange curves dissociate to the $Ca(4s4p\,^1P_1) + Yb^+(6s\,^2S_{1/2})$ and $Ca^+(4s\,^2S_{1/2}) + Yb(5d6s\,^3D_2)$ limits, respectively. Curves are labeled $|\Omega|$ and the zero of energy is located at the topmost dissociation limit. The two crossings between potentials relevant for charge transfer are indicated by circles. (b) Photon-dressed potential energies as functions of R for pathway II as defined in the text. The black curve represents the dressed-state potential dissociating to $Ca(4s^2\,^1S_0) + Yb^+(6s\,^2S_{1/2})$ plus one MOT photon. The blue curve shows the attractive potential dissociating to the $Ca(4s4p\,^1P_1) + Yb^+(6s\,^2S_{1/2})$ limit. (c) Photon-dressed potential energy curves as functions of R for pathway III. The dark-red curve shows the dressed-state potential dissociating to $Ca(4s^2\,^1S_0) + Yb^+(6s\,^2S_{1/2})$ plus one catalyst photon. The blue curve is as in (b). Black arrows in (a)–(c) indicate the entrance channel for pathways I, II, and III, respectively. The zero of energy in (b) and (c) is located at the dressed ground-state dissociation limit.

In a MOT, Ca is present in both its ground $4s^2\,^1S_0$ and its excited $4s4p\,^1P_1$ state. We then define CT pathway I as

$$Ca(^1P_1) + Yb^+(^2S_{1/2}) \rightarrow Ca^+(^2S_{1/2}) + Yb(^3D_2),$$

where the initial state is indicated by the arrow in Fig. 1(a) and pathway II as

$$\mathrm{Ca}(^1S_0) + \mathrm{Yb}^+(^2S_{1/2}) + \hbar\omega_{\mathrm{MOT}} \rightarrow \mathrm{Ca}^+(^2S_{1/2}) + \mathrm{Yb}(^3D_2).$$

This second pathway is assisted or dressed by a MOT photon with energy $\hbar\omega_{\mathrm{MOT}}$ and the $|\Omega| = 1/2$ $\mathrm{Ca}(4s4p\,^1P_1) + \mathrm{Yb}^+(6s^2S_{1/2})$ state is populated as an intermediate state, which then has CT to $\mathrm{Ca}^+ + \mathrm{Yb}$ as in the first pathway. Here, $\hbar$ is the reduced Planck constant. The MOT photon is detuned one natural line width, Γ, to the red of the Ca $^1S_0 \rightarrow {}^1P_1$ transition, leading to an avoided crossing at separations of more than a thousand Bohr radii. The repulsive excited $|\Omega| = 1/2$ and $3/2$ channels are also populated due to the laser coupling but do not lead to a significant CT reaction.

The third (III) pathway

$$\mathrm{Ca}(^1S_0) + \mathrm{Yb}^+(^2S_{1/2}) + \hbar\omega_{\mathrm{C}} \rightarrow \mathrm{Ca}^+(^2S_{1/2}) + \mathrm{Yb}(^3D_2)$$

is also photon assisted. In this case a tunable catalyst laser with frequency ω_{C} is introduced, with the goal to enhance the CT rate coefficient. The dressed ground-state potential is shown in Fig. 1(c) and crosses the same intermediate potential as in the second pathway. Here, the diabatic crossing and coupling occur at a separation R of $200a_0$ to $500a_0$. The laser is detuned to the red of the Ca $^1S_0 \rightarrow {}^1P_1$ transition by tens to hundreds of Γ.

B. Model ingredients

Conventionally one would compute CT rate coefficients for scattering from the potentials shown in Fig. 1(a), their Ω-conserving electronic couplings, and the Ω-changing (and -conserving) couplings induced by the relative atom-ion rotational interaction using a CC model. For the relevant collision energies $E = k_B \times 1\,\mathrm{mK}$ to $k_B \times 10\,\mathrm{K}$ and the long-range $1/R^3$ charge-quadruple nature of the potentials, however, contributions to the rate coefficients from a large number of total molecular angular momenta $\vec{J}$ need to be included. Here, k_B is the Boltzmann constant and $\vec{J}$ is the vector sum of the atom-ion total angular momenta and the relative mechanical orbital angular momentum $\vec{l}$, which is conserved in the absence of radiation.

To keep the computational effort tractable we employ the infinite-order sudden approximation (IOSA) [25–28], in which Coriolis couplings between different Ω states are neglected and, for a given J, uses a centrifugal potential $\hbar^2[\mathcal{L}(\mathcal{L}+1)]/(2\mu R^2)$ for each diagonal matrix element of the potential matrix. Here the integer-valued $\mathcal{L}$ is an "average" orbital angular momentum quantum number and μ is the reduced mass. We choose $\mathcal{L} = J - 1/2$ justified by the observation that for our entrance channels the sum of the atom-ion total angular momenta is $1/2$ (in units of $\hbar$). The resulting potential matrix is block diagonal in Ω, in J, and the projection M of $\vec{J}$ along the space-fixed laboratory axis. In fact, the matrix and thus the rate coefficients are independent of M. Consequently, we only need to solve for a small set of coupled Schrödinger or CC equations for each J with $M = 0$ and $\Omega = 1/2$ using standard methods [29].

Moreover, collisions on the four degenerate repulsive $|\Omega| = 1/2$ and $3/2$ $\mathrm{Ca}(4s4p\,^1P_1) + \mathrm{Yb}^+(6s\,^2S_{1/2})$ potentials will not lead to significant CT, as the reactants for our low relative collision energies are unlikely to tunnel through the $\approx hc \times 20\,\mathrm{cm}^{-1}$ barrier of these repulsive potentials. Nevertheless, these potentials will play an important role in the rate coefficient as population of the corresponding states is inevitable.

C. Diabatic coupling

Coupling between the diabatic channels is the second ingredient in setting up our CC model. Its strength is most important where potentials cross. Figure 1 shows three such points, but only two, located at $R_c = 40.7a_0$ and $42.3a_0$, respectively, lead to CT. Their coupling, in the diabatic basis which stipulates that the electronic wave functions barely change with R, comes from the overlap between the wave functions of the transferring electron on either the Ca nucleus or the Yb nucleus. Such interaction is Coulombic in nature and conserves the body-fixed projection Ω. Hence, only crossings between $|\Omega| = 1/2$ potentials are relevant. The equivalent model in the adiabatic picture would include an avoided crossing between BO potentials and a nonadiabatic coupling between them that mostly comes from the $\mathrm{d}/\mathrm{d}R$ term in the Hamiltonian acting on the overlapping adiabatic electronic wave functions.

We construct a diabatic two-channel model [21] near each $|\Omega| = 1/2$ crossing. Since the two diabatic basis functions have different electronic characters, the corresponding nonadiabatic coupling in the adiabatic picture is localized and well approximated by a Lorentzian centered at the crossing point [30]. After transformation into the diabatic picture, we can write $V_{12}(R) = [V_{11}(R) - V_{22}(R)]\tan[2\vartheta(R)]/2$, where $V_{11}(R)$ and $V_{22}(R)$ are the two diabatic potentials and mixing angle $\vartheta(R) = \arctan[(R_c - R)/R_0]/2 + \pi/4$ with crossing location R_c and coupling width R_0. [With these definitions $V_{12}(R_c) \propto R_0$.] The coupling width R_0 is taken to be the same for our two crossings and will be adjusted to lead to theoretical rate coefficients that agree with experimental values in cases where only the first two pathways are involved. The resulting coupling width is used later for all three pathways.

D. Laser-induced coupling

The MOT and catalyst lasers couple the initial photon-dressed $\mathrm{Ca}(4s^2\,^1S_0) + \mathrm{Yb}^+(6s\,^2S_{1/2}) + \hbar\omega_{\mathrm{MOT,C}}$ and excited $\mathrm{Ca}(4s4p\,^1P_1) + \mathrm{Yb}^+(6s\,^2S_{1/2})$ channels. Using a dressed-state approach [31] and in the IOSA we find coupling matrix element $-(1/\sqrt{3})d\sqrt{I/(2c\epsilon_0)}$ in SI units between the initial $\Omega = \pm 1/2$ channel and the attractive $\Omega = \pm 1/2$ excited channel with the same J.

Here, I is the MOT or catalyst laser intensity, ϵ_0 is the electric constant, dipole moment $d = \sqrt{S/3} = 2.85ea_0$, using line strength S of the $4s^2\,^1S_0$–to–$4s4p\,^1P_1$ transition of Ca [32], and e is the electron charge. The factor $1/\sqrt{3}$ accounts for the polarization of the laser projected onto the body-fixed coordinate frame. Direct laser-induced couplings between the ground $\Omega = \pm 1/2$ and the attractive excited $\mp 1/2$ channels do not occur. This is because in the body-fixed frame, the attractive excited channel has $\Omega_{\mathrm{Ca}} = 0$ and the transition preserves the projection quantum number of Yb due to the fact that the transition dipole moment in the long range (where the transition is most likely to happen) originates from the

excitation of outer electrons of the Ca atom. The lasers also couple the ground-state channel to repulsive excited $|\Omega| = 1/2$ and $3/2$ channels. The repulsive channels, however, do not significantly contribute to the charge-transfer process and their laser-induced coupling matrix elements are not required.

Laser-induced couplings persist to $R \to \infty$ and for pathways II and III we must diagonalize the asymptotic potential matrix and use its eigenvectors and the average partial-wave quantum number $\mathcal{L}$ to define a dressed scattering basis. For pathway I, where light does not dress states, the original atomic basis states can be used. For each of the three pathways we can then solve the CC equation for $|\Omega| = 1/2$ and each $\mathcal{L}$ (or, equivalently, J) and compute the CT cross section $\sigma_i(E, \mathcal{L})$ for $i =$ I, II, and III and relative kinetic energy E of the corresponding initial state. The multiplicity factor of $(2\mathcal{L} + 1)$ is included in obtaining the cross section.

E. Spontaneous decay

Charge transfer involving the excited $\mathrm{Ca}(4s4p\,^1P_1)$ state is affected by spontaneous emission [33–35], which limits the probability of colliding particles remaining in the excited channel and reaching the diabatic crossing region near $R \approx 40a_0$, where CT is most likely to occur. For our first pathway, $\mathrm{Ca}(4s4p\,^1P_1)$ and $\mathrm{Yb}^+(6s\,^2S_{1/2})$ start at very large R. For the second and third pathways the excitation to the intermediate $\mathrm{Ca}(4s4p^1P_1) + \mathrm{Yb}^+(6s\,^2S_{1/2})$ state is resonant at separations where the energy of the $|\Omega| = 1/2$ ground-state potential plus the energy of a laser photon equals the attractive $|\Omega| = 1/2$ of the intermediate channel as shown in Figs. 1(b) and 1(c). This occurs at $R \approx 1200a_0$ for pathway II and between $200a_0$ and $500a_0$ for pathway III, depending on detuning. The classical time for the atom and ion to be pulled together to separations near R_c by the attractive excited potentials at ultracold collision energies can approach or exceed the $\tau = 4.59$ ns $\mathrm{Ca}(4s4p\,^1P_1)$ lifetime.

We account for this spontaneous decay by computing the survival probability $p_i(E, \mathcal{L})$ of reaching crossing points R_c for the initial collision energy E and average partial wave $\mathcal{L}$ for each pathway i [36]. In essence, the probability is based on computing the collision time along classical trajectories on the attractive excited $\mathrm{Ca}(4s4p\,^1P_1) + \mathrm{Yb}^+(6s\,^2S_{1/2})$ $|\Omega| = 1/2$ potential. More details are given in Appendix A. The cross section obtained from the CC calculation and the survival probability are combined to define the total CT rate coefficient

$$k_i(E) = f_i \sum_{\mathcal{L}=0}^{\infty} p_i(E, \mathcal{L})\, v_{\mathrm{rel}} \sigma_i(E, \mathcal{L}) \qquad (1)$$

for $i =$ I, II, and III, where $v_{\mathrm{rel}} = \sqrt{2E/\mu}$ is the absolute value of the relative velocity $\vec{v}_{\mathrm{rel}}$. The factor $f_i = \eta/3$, $1 - \eta$, and $1 - \eta$ for $i =$ I, II, and III, respectively. For pathway I it accounts for the fact that in a MOT a fraction η of the Ca atoms is in the exited state and that only the two (degenerate) attractive $|\Omega| = 1/2$ $\mathrm{Ca}(4s4p\,^1P_1) + \mathrm{Yb}^+(6s\,^2S_{1/2})$ channels of the six excited states lead to CT. For pathways II and III f_i is simply the fraction of Ca atoms in the ground state, as both initial states, $\Omega = \pm 1/2$, equally contribute to the CT rate coefficient. We use the MOT parameter in Ref. [37], which leads to $\eta = 0.092$, in our calculations.

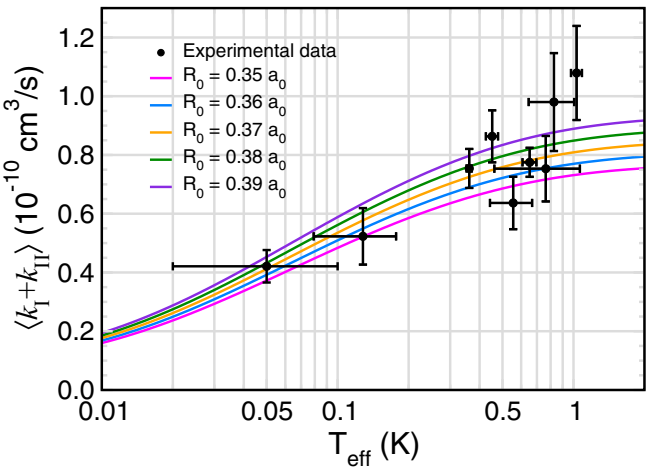

FIG. 2. Total thermalized charge-transfer rate coefficient in a Ca MOT as a function of the effective temperature T_{eff} in the center-of-mass frame. Filled black circles with one-standard-deviation error bars are our experimental data points. Solid lines are theoretical predictions with coupling width R_0 ranging from $0.35a_0$ to $0.39a_0$. The MOT laser has an intensity of 78 mW/cm^2 and is red detuned from the Ca $^1S_0$-to-$^1P_1$ transition by one natural line width, such that 9.2% of the Ca atoms are in the $^1P_1$ state.

As the ion temperature T_{i} is much higher than that of the atoms, the relative velocity distribution in the center-of-mass frame can be described by the three-dimensional Gaussian probability distribution $P(\vec{v}_{\mathrm{rel}}) \propto \exp(-\mu v_{\mathrm{rel}}^2/[2k_B T_{\mathrm{eff}}])$ with effective temperature $T_{\mathrm{eff}} = m_{\mathrm{Ca}} T_{\mathrm{i}}/M$, $M = m_{\mathrm{Ca}} + m_{\mathrm{Yb}}$, and Ca and Yb^+ masses m_{Ca} and m_{Yb}, respectively. We use this distribution to thermally average the CT rate coefficient.

III. RESULTS

A. Pathways I and II: MOT-induced charge transfer

Figure 2 compares our total charge-transfer rate coefficients as measured in the MOT with the thermalized theoretical $\langle k_{\mathrm{I}}(E) + k_{\mathrm{II}}(E)\rangle$ for several values of R_0 as a function of the effective temperature T_{eff} between 0.01 and 2 K. The data show a significant decrease in the rate coefficient due to the suppression from spontaneous decays as the temperature decreases by over an order of magnitude. Additional analysis shows that about 40% of the theoretical rate coefficient is due to the first pathway. The figure also shows that at a fixed temperature the rate coefficient increases monotonically when the coupling width R_0 increases from $0.35a_0$ to $0.39a_0$. The theoretical values agree well with the experimental data. The coupling strength $V_{12}(R = R_c)$ for these R_0 at the crossing points is approximately $hc \times 0.5$ cm^{-1}. In support of the theoretical model, we obtained comparable coupling strengths near R_c and thus comparable R_0's with a Heitler-London type of estimate [38], discussed in detail in Appendix A, using the overlap integral of Hartree-Fock atomic orbitals and the electron-nucleus Coulomb interaction potential.

B. Pathway III: Photoassociation-enhanced charge transfer

In the experiment described in Ref. [37] the addition of a tunable laser with intensity I_{C} and (angular) frequency ω_{C}

enhances the charge-transfer processes as the third pathway is added. This laser is detuned to the red of the Ca $^1S_0$-to-$^1P_1$ transition by tens to hundreds of natural line widths. In fact, the laser excites rovibrational levels of the attractive $|\Omega| = 1/2$ Ca$(4s4p\,^1P_1) + $ Yb$^+(6s\,^2S_{1/2})$ potential. Since the MOT cooling lasers in the experiment are always on, the third pathway coexists with the other two.

In this paper we want to highlight and focus on the effect of the catalyst laser. The relevant diabatic potentials are shown in Figs. 1(a) and 1(c). The potential matrix including the R-independent laser-induced couplings is diagonalized at large R for each $\mathcal{L}$. Its eigenvectors are the appropriate scattering basis states under the IOSA with which to calculate scattering amplitudes and cross sections. By solving the CC equations, we obtain the partial cross sections for the third pathway, $\sigma_{\rm III}(E, \mathcal{L}, \omega_{\rm pa})$. The survival probability $p_{\rm III}(E, \mathcal{L}, \omega_{\rm C})$ is higher than for the second pathway. This is because the crossing between the dressed entrance channel and the intermediate excited channel occurs at $R \sim 200a_0 - 500a_0$, depending on $\omega_{\rm C}$, which is much smaller than for the second pathway. Thus, the reactants are quickly accelerated along the excited attractive $1/R^3$ potential and need much less time to reach R_c to react.

The addition of pathway III via the catalyst laser enhances the charge-transfer reaction by adding $k_{\rm III}(E)$ to the total rate coefficient $k_{\rm tot}(E)$, while leaving $k_{\rm I}(E)$ and $k_{\rm II}(E)$ unchanged to good approximation. Similarly, we find thermally averaged rate coefficients $k_{\rm tot}(T)$. The theoretical $k_{\rm tot}(T)$ based on $R_0 = 0.37(2)a_0$ is compared with our experimental rate coefficients as a function of the catalyst laser detuning and intensity in Fig. 4 of the accompanying paper [37]. The agreement is satisfactory and we conclude that we can predict CT rate coefficients with and without a catalyst laser as well as its temperature dependence with a single consistent value for R_0.

In the remainder of this section we present a study of CT in the presence of the catalyst laser in more detail. Figure 3 shows an example of $k_{\rm III}(E)$ as a function of the laser detuning at collision energy $E = k_B \times 1\,$mK. It is evident that the charge-transfer reaction occurs in a resonant fashion with a larger number of narrow peaks. The resonance locations cluster and correspond to rotational progressions of the vibrational series of the attractive $|\Omega| = 1/2$ potential dissociating to the Ca$(4s4p\,^1P_1) + $ Yb$^+(6s\,^2S_{1/2})$ threshold. The height of the resonant features decrease with increasing (negative) detuning as the overlap of resonances decreases due to increasing rovibrational spacing in the excited potential.

Scattering from 13 partial waves $\mathcal{L}$ contribute significantly to the CT as the 1-mK collision energy roughly corresponds to the height of the centrifugal barrier for the $\mathcal{L} = 12$ channel. To illustrate this, we compare the locations of the resonances with the rovibrational bound states of the attractive *diabatic* potential dissociating to the Ca$(4s4p\,^1P_1) + $ Yb$^+(6s\,^2S_{1/2})$ threshold in Fig. 3. The figure also shows the expected value of $\mathcal{L}$ for each resonance. In Fig. 3(a), the locations of the onset of each group of resonances closely follow the binding energies of rovibrational series.

Figure 3(b) shows a blowup of the spectrum for three vibrational levels in Fig. 3(a). We see that the location of rotational states $\mathcal{L}$ does not directly follow the location of the corresponding resonances. The shifts are due to interferences with the charge-transferred Ca$^+(^2S) + $ Yb$(^3D_2)$ exit channels induced by the nonperturbative short-range couplings.

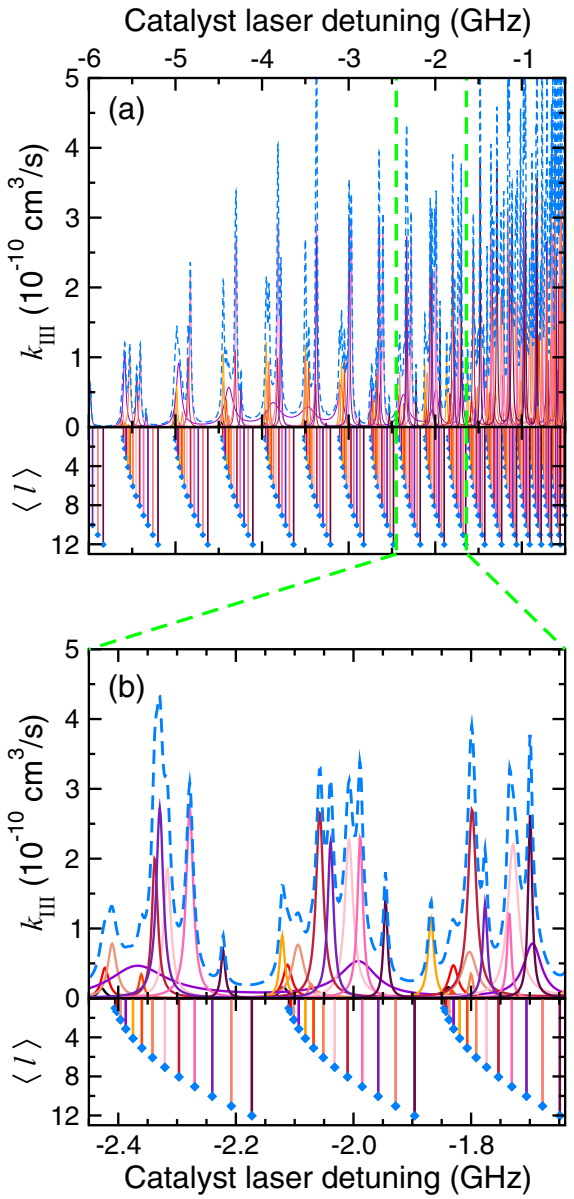

FIG. 3. Charge-transfer rate coefficients from the catalyst laser and assignment of catalyst resonances as functions of the detuning from the Ca $^1S_0$-to-$^1P_1$ transition for collision energy $E = k_{\hat{B}} \times 1\,$mK, laser intensity $I_{\rm C} = 5\,$W/cm^2, and coupling width $R_0 = 0.37a_0$. (a) The upper panel shows rate coefficients for detunings between -6 and $-0.5\,$GHz; (b) the upper panel shows a blowup near $-2\,$GHz in order to better distinguish the different curves. The dashed blue line corresponds to the total rate coefficient from pathway III, while the various-colored solid lines represent contributions from average partial-wave channels $\mathcal{L} = 0$ to 12. The lower panel in (a) and (b) shows the rovibrational $\Omega = 1/2$ bound states dissociating to the Ca$(4s4p\,^1P_1) + $ Yb$^+(6s\,^2S_{1/2})$ threshold. The lowest 13 rotational states for each vibrational state are shown and the colors of the drop lines mimic the colors of the $\mathcal{L}$ contributions in the upper panels. The y axis in the lower panels is the expectation value of $\vec{\mathcal{L}}$ of the bound states.

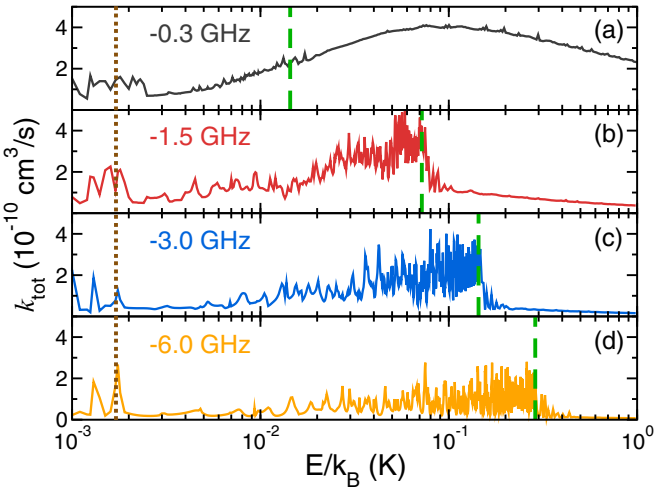

FIG. 4. Total charge-transfer rate coefficients in the presence of the catalyst laser as functions of the collision energy E. The photoassociation laser is detuned (a) 0.3 GHz, (b) 1.5 GHz, (c) 3.0 GHz, and (d) 6.0 GHz to the red of the Ca $^1S_0$-to-$^1P_1$ transition. In each panel the vertical dashed green line represents a collision energy equal to the energy equivalent of the detuning of the catalyst laser. The vertical dotted brown line is located at $E = h\Gamma = k_B \times 1.7\,\mathrm{mK}$, both the energy equivalent of the MOT laser detuning and the natural line width of the Ca $^1P_1$ state. We assume a catalyst laser intensity $I_C = 6\ \mathrm{W/cm^2}$ and coupling width $R_0 = 0.39a_0$.

Figure 4 shows an example total CT rate coefficient $k_{tot}(E)$ as a function of the collision energy at four detunings, δ, of the catalyst laser. The laser intensity is two orders of magnitude larger than I_{MOT}. For $\delta = -0.3\,\mathrm{GHz}$, $k_{tot}(E)$ shows a smooth behavior, interlaced with weak narrow features, and a maximum near $E = k_B \times 0.1\,\mathrm{K}$. For larger detunings sharp features dominate, while above a critical collision energy the rate coefficient rapidly approaches 0. For all detunings strong resonances are visible for $E < k_B \times 2\,\mathrm{mK}$.

The behavior for large catalyst laser detunings can be understood from comparison of the collision energy with $h\delta$, the dashed green lines in Fig. 4. For $E < h\delta$ pathway III contributes resonances to the total rate coefficient due to the coupling between the entrance channel continuum and the bound states of the attractive intermediate $|\Omega| = 1/2$ potential. When the collision energy exceeds $h\delta$, the entrance continuum is only coupled to scattering states of the intermediate channel. Their coupling matrix elements are much smaller than those between continuum-bound states and the rate coefficient becomes much smaller.

For $\delta = -0.3\,\mathrm{GHz}$, the total rate coefficient does not turn off at $h\delta$ thanks to pathway III as a consequence of the fact that for small detunings the energy spacing between excitable vibrational levels is smaller and resonances begin to overlap. In fact, helped by the relatively high-powered catalyst laser, interference between the broadened resonances becomes important. Hence, the resonances behave almost like a continuum and the rate coefficient is a smooth function of E for energies both lower and higher than $h\delta$. The same effect is not obvious for the MOT laser pathway due to the much lower laser intensity, which couples the continuum and the bound states much more weakly and does not broaden the resonances nearly as much despite the smaller detuning.

Finally, pathway II contributes resonances to the total rate coefficient for collision energies comparable to or lower than $k_B \times 2\,\mathrm{mK}$, roughly corresponding to the detuning of the MOT laser $h\Gamma = k_B \times 1.7\,\mathrm{mK}$ labeled by the dashed brown lines. These resonances correspond to bound states with extremely long-range outer turning points in the intermediate $|\Omega| = 1/2$ potential.

Currently, our experiments cannot resolve the resonances illustrated in Figs. 3 and 4 due to the relatively broad velocity distribution of the ions. Once better energy selectivity can be achieved and resonances resolved experimentally, the ground and excited potentials can be theoretically adjusted such that detunings of resonances from specific excited vibrational manifolds as well as the corresponding line strength pattern agree with the experimental data. The energy dependence shown in Fig. 4 could be observed by accelerating clouds of ultracold neutral Ca atoms at an ion cloud of a similar temperature [39].

IV. CONCLUSION

In conclusion, we have presented experimental measurements and results from a close-coupling model of photon-induced charge transfer in $Ca + Yb^+$ that yield insight into three contributing reaction mechanisms. The model relies on a dense manifold of electronically excited long-range induction and dipolar potentials, their nonadiabatic coupling, and the survival probabilities against spontaneous emission of the excited Ca atom. It leads to a high charge-transfer rate coefficient, of the order of 10^{-11}–10^{-10} cm^3/s, in agreement with the experimental results [37].

We have shown that the near-degeneracy of the excited $Ca(^1P_1) + Yb^+(^2S)$ and $Ca^+(^2S) + Yb(^3D_2)$ asymptotic limits leads to large charge-transfer rate coefficients that can be controlled by changing the frequency of the catalyst laser. A coupled-channels model, using the long-range interaction potentials of, as well as the couplings among, these states, with just a single adjustable coupling strength, R_0, can reproduce all experimental data, with and without the catalyst laser, as a function of the temperature. Our theoretical Heitler-London-type estimate of the coupling strength agrees with the fitted value.

We have also presented predictions for future experiments on charge transfer in Ca and Yb^+ collisions. We have shown that a complex resonance spectrum can be observed as the catalyst laser is scanned over just $\Delta = 6\,\mathrm{GHz}$ to the red of the $Ca(^1S_0)$–to–$Ca(^1P_1)$ line. Similarly, we predict that changing the collision energy between the atoms and the ions can significantly change the charge-transfer rate coefficient in a resonant fashion.

ACKNOWLEDGMENTS

Work at the Temple University was supported by MURI Army Research Office Grants No. W911NF-14-1-0378 and No. W911NF-17-1-0563, U.S. Air Force Office of Scientific Research Grant No. FA9550-14-1-0321, and NSF Grant No. PHY-1619788. Work at UCLA was supported in part by

National Science Foundation (Grants No. PHY-1255526, No. PHY-1415560, and No. DGE-1650604) and Army Research Office (Grants No. W911NF-15-1-0121, No. W911NF-14-1-0378, and No. W911NF-13-1-0213).

APPENDIX A: LONG-RANGE INTERACTION POTENTIALS

We now describe in more detail the long-range diabatic interaction potentials between excited Ca and Yb^+ coupled to Ca^+ and excited Yb as shown in Fig. 1(a). The interaction between an excited atom and an ion has two contributions. The first arises from the interaction between the ion charge and the quadrupole moment of the excited atom and has an anisotropic C_3/R^3 dependence on atom-ion separation $\vec{R}$, where C_3 depends on the orientation of $\vec{R}$. The second term is an anisotropic C_4/R^4 interaction, where C_4 also depends on the orientation of $\vec{R}$. It originates in second-order perturbation theory from the interaction between the charge and the induced dipole moment of the neutral atom. Consequently, both C_3 and C_4 depend only on the properties of the neutral atom.

Our diabatic potentials are the diagonal matrix elements of the molecular interaction in the atomic basis in the body-fixed frame $|q_a j_a \Omega_a, q_b j_b \Omega_b\rangle = |q_a, j_a \Omega_a\rangle |q_b, j_b \Omega_b\rangle$ labeled by charge state $q_s = 0, +1$ and body-fixed projection quantum number Ω_s of the angular momentum j_s of the atom or ion along the internuclear axis, where $s = a$ and b for Ca and Yb, respectively. This uniquely labels the atomic states relevant for our system. Electronic molecular interactions always conserve $\Omega = \Omega_a + \Omega_b$.

Crucially, for our system both contributions to the long-range potential are diagonal in this body-fixed basis [31]. The matrix elements of C_3, expressed in two equivalent ways, are

$$C_{3,j_s\Omega_s} = q\frac{\langle j_s\Omega_s | j_s 2\Omega_s 0\rangle}{\langle j_s j_s | j_s 2 j_s 0\rangle}\frac{Q}{2}$$
$$= q(-1)^{j_s-\Omega_s}\begin{pmatrix} j_s & 2 & j_s \\ -\Omega_s & 0 & \Omega_s\end{pmatrix}\langle j_s||Q_2||j_s\rangle,$$

where the quantum numbers $j_s\Omega_s$ always describe the state of the neutral atom, $q = +1$ for the corresponding ion, (:::) denotes a Wigner 3-j symbol, and $\langle j_1 m_1 | j_2 j_3 m_2 m_3\rangle$ is a Clebsch-Gordan coefficient. Finally, Q is the quadrupole moment defined in Refs. [40,41], while $\langle j_s||Q_2||j_s\rangle$ is the reduced matrix element used in Refs. [41,42]. For the $^1P_1$ Ca state the quadrupole moment is positive with $|Q| = 11.04ea_0^2$ [40]. The sign convention is derived from Ref. [43]. For the $^3D_2$ state of Yb, $\langle j_s||Q_2||j_s\rangle = +14.2ea_0^2$ [42].

The diagonal matrix elements of the C_4 coefficient are [44]

$$C_{4,j_s\Omega_s} = -\frac{q^2}{2}\left[\alpha_{0,j_s} + \alpha_{2,j_s}\frac{3\Omega_s^2 - j_s(j_s+1)}{j_s(2j_s-1)}\right],$$

where α_{0,j_s} is the static scalar polarizability and α_{2,j_s} is the static tensor polarizability of the neutral atom in state $|0, j_s\Omega_s\rangle$. For the Ca $^1P_1$ state, $\alpha_{0,1} = 242.4a_0^3$ and $\alpha_{2,1} = -55.3a_0^3$ [40]. For the Yb $^3D_2$ state, $\alpha_{0,2} = 61a_0^3$ and $\alpha_{2,2} = 28a_0^3$ [42,45].

Finally, the long-range interaction between a neutral S-state atom and an S-state ion has an isotropic, attractive C_4/R^4 dependence on R. For $Ca + Yb^+$ it is shown in Figs. 1(b) and 1(c) as the dressed-state potential. The C_4 coefficient equals $-\alpha_{0,0}/2$, where $\alpha_{0,0}$ is the static polarizability of the neutral atom. The C_3 coefficient is 0, as S-state atoms have zero quadrupole moment.

TABLE I. C_3 and C_4 coefficients of the attractive long-range $\Omega = 1/2$ diabatic potentials in atomic units and quantum numbers for the corresponding $Ca + Yb^+$ and $Ca^+ + Yb$ channels. Channels are uniquely described by the charge q_i, the atomic angular momenta j_i, and the body-fixed projection Ω_i on the internuclear axis, with $i = a$ and b for Ca and Yb, respectively. Potentials are degenerate for $-\Omega$ and Ω, where $\Omega = \Omega_a + \Omega_b$.

Ca/Ca^+			Yb/Yb^+				
q_a	j_a	Ω_a	q_b	j_b	Ω_b	C_3	C_4
0	0	0	+1	1/2	1/2	0	−78.55
0	1	0	+1	1/2	1/2	−11.04	−176.74
+1	1/2	1/2	0	2	0	−3.39	−16.5
+1	1/2	−1/2	0	2	1	−1.70	−23.5

Table I lists the relevant C_3 and C_4 coefficients as well as the quantum numbers of the channels. A negative sign indicates attractive interactions. At smaller separations (not shown in Fig. 1) each potential transitions to a repulsive C_{12}/R^{12} potential.

Diabatic potentials with the same Ω cross and couple near $R_c \approx 40a_0$. As discussed in the text, we have opted to use model coupling function with coupling width R_0. The value of R_0 is fitted to experimental data and estimated to be between 0.35 and $0.39\,a_0$. In support of our model and fitting result, we can also estimate the diabatic coupling strength at $R = R_c$ based on a Heitler-London method. In atomic units, we can write the coupling matrix element between the attractive $|\Omega| = 1/2 Ca(4s4p\,^1P_1) + Yb^+(6s\,^2S_{1/2})$ and $Ca^+(4s\,^2S_{1/2}) + Yb(5d6s\,^3D_2)$ channels as

$$V_{12}(R) \sim \langle Ca(4p)|\frac{1}{r_{Ca}} + \frac{1}{r_{Yb}}|Yb(5d)\rangle, \qquad (A1)$$

where $|Ca(4p)\rangle$ and $|Yb(5d)\rangle$ are the Ca $4p$ and Yb $5d$ Hartree-Fock electronic orbitals, respectively, and the electron coordinate for the two orbitals is $\vec{r}_{Ca,Yb}$ with respect to the Ca and Yb nuclei, respectively. At $R = 41a_0$, the method yields $V_{12,HL}(R) \sim hc \times 0.27\ cm^{-1}$, which corresponds to the range of $R_0 = 0.37(2)a_0$ we obtained.

APPENDIX B: SURVIVAL PROBABILITIES

The evaluation of survival probabilities within the IOSA framework on the attractive excited potential $V_e(R)$ of the $|\Omega| = 1/2\ Ca(4s4p\,^1P_1) + Yb^+(6s\,^2S_{1/2})$ channel due to spontaneous decay of the Ca $^1P_1$ state can be treated with rate equations for populations derived from the optical Bloch equations [36,46]. Here, the atom pair decays back to the ground-state potential $V_g(R)$ of the $|\Omega| = 1/2\ Ca(4s^2\,^1S_0) + Yb^+(6s\,^2S_{1/2})$ channel. In a MOT we can assume that the coherence between the Ca $^1S_0$ and the Ca $^1P_1$ states decays much more rapidly than those of the populations. Moreover, at our temperatures where a large number of relative orbital

angular momenta $\mathcal{L}$ contribute, the relative nuclear motion for the purpose of estimating the survival probability can be described by classical evolution $R(t)$ on the potential $U_e(R;\mathcal{L}) = V_e(R) + \hbar^2\mathcal{L}(\mathcal{L}+1)/(2\mu R^2)$ from the excitation region at (very) large separation at $t = 0$ to $R_c \approx 40a_0$, the separation where charge transfer occurs. At $t = 0$ the atom pair has relative kinetic energy E and is moving towards smaller R.

Under these assumptions we have for pathway I

$$\frac{\mathrm{d}p_e(t)}{\mathrm{d}t} = -\Gamma p_e(t) - \Gamma'(t)\, p_e(t) + \frac{1}{3}\Gamma'(t)\, p_g(t) \qquad \text{(B1)}$$

and $p_g(t) + 3p_e(t) = 1$, where $p_g(t)$ and $p_e(t)$ are the populations in the ground- and excited-state channels, respectively. Here, Γ is the natural line width of Ca($^1P_1$), and

$$\Gamma'(t) = A_\Gamma \frac{\gamma^3}{\Delta E(t)^2 + \gamma^2} \qquad \text{(B2)}$$

describes the stimulated absorption and emission rate of MOT photons, where $\gamma = \Gamma/2$ and the time-dependent $\Delta E(t) = V_e(R(t)) - V_g(R(t)) - \hbar\omega_{\mathrm{MOT}}$ at separation $R(t)$. The last term on the right-hand side of Eq. (B1) accounts for processes where, after a spontaneous emission event, the atom pair is again excited and participates in the charge-transfer collision. The factor of one-third in this term accounts for the fact that only one-third of the photons are able to excite the system back to the attractive excited channels.

The constant A_Γ is set such that the steady-state solution of Eq. (B1) for $R \to \infty$ reproduces the experimental fraction of atom pairs in the $|\Omega| = 1/2$ excited potential $V_e(R)$, i.e., $p_e|_{R\to\infty} = \eta/3$, where η is the fraction of Ca atoms in the $^1P_1$ state. For the MOT parameters in Ref. [37] $\Delta E \to -\Gamma$ for $R \to \infty$ and $\eta = 0.092$.

In practice, we do not solve Eq. (B1) directly but rephrase the equation into one for separation R by noting that $\mathrm{d}t = \mathrm{d}R/v(R;E,\mathcal{L})$, where the velocity $v(R;E,\mathcal{L})$ satisfies $\mu v^2/2 + U_e(R;\mathcal{L}) = E$ for each R. The radial differential equation can be integrated from very large R to crossing point R_c to obtain the survival probability $p_{\mathrm{I}}(E,\mathcal{L})$ for pathway I.

Our second pathway is also affected by spontaneous decay of the excited channels. In this case the excitation occurs near $R_x \approx 1200a_0$. The stimulated excitation and decay are already included in the close-coupling calculations when the light coupling is included and the asymptotic basis functions diagonalized and, thus, do not need to be included here. We then find the simpler differential equation

$$\frac{\mathrm{d}p_e(t)}{\mathrm{d}t} = -\Gamma p_e(t), \qquad \text{(B3)}$$

which is transformed into one for R and solved from $R = R_x$ with $p_e(R_x) = 1$ to R_c assuming an initial kinetic energy E and average partial wave $\mathcal{L}$. The final value at R_c defines the survival probability $p_{\mathrm{II}}(E,\mathcal{L})$ for this pathway. The differential equation for the third pathway is the same as for pathway II, but now the excitation separation is even smaller and we find that the $p_{\mathrm{III}}(E,\mathcal{L})$ are larger than 0.1 for the detunings considered here.

[1] R. Coté and A. Dalgarno, Phys. Rev. A **62**, 012709 (2000).
[2] A. Watanabe, C. M. Dutta, P. Nordlander, M. Kimura, and A. Dalgarno, Phys. Rev. A **66**, 044701 (2002).
[3] L. B. Zhao, P. C. Stancil, J. P. Gu, H. Liebermann, Y. Li, P. Funke, R. J. Buenker, B. Zygelman, M. Kimura, and A. Dalgarno, Astrophys. J. **615**, 1063 (2004).
[4] A. T. Grier, M. Cetina, F. Oručević, and V. Vuletić, Phys. Rev. Lett. **102**, 223201 (2009).
[5] P. Zhang, E. Bodo, and A. Dalgarno, J. Phys. Chem. A **113**, 15085 (2009).
[6] Z. Idziaszek, T. Calarco, P. S. Julienne, and A. Simoni, Phys. Rev. A **79**, 010702(R) (2009).
[7] C. Zipkes, S. Palzer, L. Ratschbacher, C. Sias, and M. Köhl, Phys. Rev. Lett. **105**, 133201 (2010).
[8] S. Schmid, A. Härter, and J. H. Denschlag, Phys. Rev. Lett. **105**, 133202 (2010).
[9] F. H. J. Hall, M. Aymar, N. Bouloufa-Maafa, O. Dulieu, and S. Willitsch, Phys. Rev. Lett. **107**, 243202 (2011).
[10] X. J. Liu, Y. Z. Qu, B. J. Xiao, C. H. Liu, Y. Zhou, J. G. Wang, and R. J. Buenker, Phys. Rev. A **81**, 022717 (2010).
[11] P. Zhang, A. Dalgarno, R. Cote, and E. Bodo, Phys. Chem. Chem. Phys. **13**, 19026 (2011).
[12] M. Tacconi, F. A. Gianturco, and A. K. Belyaev, Phys. Chem. Chem. Phys. **13**, 19156 (2011).
[13] W. G. Rellergert, S. T. Sullivan, S. Kotochigova, A. Petrov, K. Chen, S. J. Schowalter, and E. R. Hudson, Phys. Rev. Lett. **107**, 243201 (2011).
[14] H. D. L. Lamb, J. F. McCann, B. M. McLaughlin, J. Goold, N. Wells, and I. Lane, Phys. Rev. A **86**, 022716 (2012).
[15] A. K. Belyaev, S. A. Yakovleva, M. Tacconi, and F. A. Gianturco, Phys. Rev. A **85**, 042716 (2012).
[16] E. R. Sayfutyarova, A. A. Buchachenko, S. A. Yakovleva, and A. K. Belyaev, Phys. Rev. A **87**, 052717 (2013).
[17] B. M. McLaughlin, H. D. L. Lamb, I. Lane, and J. F. McCann, J. Phys. B **47**, 145201 (2014).
[18] S. Haze, R. Saito, M. Fujinaga, and T. Mukaiyama, Phys. Rev. A **91**, 032709 (2015).
[19] S. T. Sullivan, W. G. Rellergert, S. Kotochigova, and E. R. Hudson, Phys. Rev. Lett. **109**, 223002 (2012).
[20] P. Puri, M. Mills, C. Schneider, I. Simbotin, J. A. Montgomery, R. Côté, A. G. Suits, and E. R. Hudson, Science **357**, 1370 (2017).
[21] E. E. Nikitin, in *Springer Handbooks of Atomic, Molecular, and Optical Physics*, edited by G. W. F. Drake (Springer, New York, 2006), pp. 741–752.
[22] B. Zygelman, Z. Lucic, and E. R. Hudson, J. Phys. B: At. Mol. Opt. Phys. **47**, 015301 (2014).
[23] M. Tomza, C. P. Koch, and R. Moszynski, Phys. Rev. A **91**, 042706 (2015).
[24] B. Gao, Phys. Rev. A **83**, 062712 (2011).
[25] R. T. Pack, J. Chem. Phys. **60**, 633 (1974).
[26] D. Secrest, J. Chem. Phys. **62**, 710 (1975).
[27] L. W. Hunter, J. Chem. Phys. **62**, 2855 (1975).
[28] D. J. Kouri, in *Atom–Molecule Collision Theory*, edited by R. B. Bernstein (Springer, New York, 1979), pp. 301–358.
[29] R. G. Gordon, J. Chem. Phys. **51**, 14 (1969).
[30] H. Werner and W. Meyer, J. Chem. Phys. **74**, 5802 (1981).

[31] A. Petrov, C. Makrides, and S. Kotochigova, J. Chem. Phys. **146**, 084304 (2017).
[32] Y. Yu and A. Derevianko, At. Data Nucl. Data Tables **119**, 263 (2018).
[33] A. Gallagher and D. E. Pritchard, Phys. Rev. Lett. **63**, 957 (1989).
[34] P. Julienne, A. Smith, and K. Burnett, in *Advances In Atomic, Molecular, and Optical Physics*, edited by D. Bates and B. Bederson (Academic Press, 1992), pp. 141–198.
[35] H. M. J. M. Boesten, B. J. Verhaar, and E. Tiesinga, Phys. Rev. A **48**, 1428 (1993).
[36] K.-A. Suominen, M. J. Holland, K. Burnett, and P. S. Julienne, Phys. Rev. A **49**, 3897 (1994).
[37] M. Mills, P. Puri, M. Li, S. J. Schowalter, A. Dunning, C. Schneider, S. Kotochigova, and E. R. Hudson, Phys. Rev. Lett. **122**, 233401 (2019).
[38] K. Tang, J. P. Toennies, and C. L. Yiu, Int. Rev. Phys. Chem. **17**, 363 (1998).
[39] R. Thomas, M. Chilcott, E. Tiesinga, A. B. Deb, and N. Kjærgaard, Nat. Commun. **9**, 4895 (2018).
[40] J. Mitroy and J.-Y. Zhang, J. Chem. Phys. **128**, 134305 (2008).
[41] A. Derevianko, Phys. Rev. Lett. **87**, 023002 (2001).
[42] A. A. Buchachenko, Eur. Phys. J. D **61**, 291 (2011).
[43] S. C. Ceraulo and R. S. Berry, Phys. Rev. A **44**, 4145 (1991).
[44] J. Mitroy, M. S. Safronova, and C. W. Clark, J. Phys. B: At. Mol. Opt. Phys. **43**, 202001 (2010).
[45] C. J. Bowers, D. Budker, S. J. Freedman, G. Gwinner, J. E. Stalnaker, and D. DeMille, Phys. Rev. A **59**, 3513 (1999).
[46] C. Cohen-Tannoudji, J. Dupont-Roc, and G. Grynberg, *Atom-Photon Interactions* (Wiley-Blackwell, 2008), pp. 353–405.